Journal of Electroanalytical Chemistry 1005 (2026) 119870

Contents lists available at ScienceDirect

Journal of Electroanalytical Chemistry

journal homepage: www.elsevier.com/locate/jelechem

Correlation between spinel structure and electrochemical kinetic behavior of spinel ferrites

Meng Sun [a,1], Guanting Liu [a,1], Shujin Hao [a], Feiyu Diao [b], Federico Rosei [c], Rongsheng Cai [d,*], Yiqian Wang [a,*]

[a] College of Physics, Qingdao University, No. 308 Ningxia Road, Qingdao 266071, PR China
[b] Industrial Research Institute of Nonwovens & Technical Textiles, Shandong Center for Engineered Nonwovens, College of Textiles & Clothing, Qingdao University, No. 308 Ningxia Road, Qingdao 266071, PR China
[c] Department of Chemical and Pharmaceutical Sciences, University of Trieste, Via Giorgeri 1, 34127 Trieste, Italy
[d] State Key Laboratory of Solid Lubrication, Lanzhou Institute of Chemical Physics, Chinese Academy of Sciences, Lanzhou 730000, PR China

ARTICLE INFO

Keywords:
Lithium-ion batteries
Electrospinning
Spinel structure
Microstructure
Electrochemical performance

ABSTRACT

Recent studies have shown that spinel ferrites featuring unique spinel structures are promising as anode materials in lithium-ion batteries (LIBs) because of their high capacity, low cost, and abundant resources. However, the influence of the spinel structure on the electrochemical properties of spinel ferrites is still poorly understood. Herein, three different spinel ferrites, namely, normal spinel $ZnFe_2O_4$, mixed spinel $MgFe_2O_4$, and inverse spinel $CoFe_2O_4$ nanofibers are prepared by electrospinning, aiming to correlate the spinel structure with their electrochemical kinetic behavior. It is found that the spinel type of spinel ferrites is associated with the initial voltage platform in the discharge process and reaction kinetics. As an anode for LIBs, the ZFO electrode demonstrates the highest initial voltage platform and superior lithium-ion transport capability. This is mainly attributed to the large proportion of Fe^{3+} occupying octahedral sites in the normal spinel, which facilitates the migration of lithium ions into the lattice of the anode. This work advances the understanding of the effects of spinel structure on the battery performance, enabling the targeted synthesis of optimized materials for enhanced performance of LIBs.

1. Introduction

The scientific community increasingly focuses on energy storage solutions for renewable resources [1–6]. Lithium-ion batteries (LIBs) are recognized as a leading technology in this field and are extensively used in portable electronics, electric cars, and smart grids [7–11]. Spinel ferrites, adopting a general molecular formula of MFe_2O_4 (M = Mn, Mg, Co, Cu, Zn, Ni) [12–16], are considered promising anode materials for LIBs. Based on the cation distribution at octahedral and tetrahedral sites, the spinel structure can be classified into normal, mixed and inverse, imparting spinel ferrites with diverse physical and chemical properties. For example, the spinel structure is closely correlated with the catalytic performance of spinel ferrites [18–20]. However, up to now, the influence of cation distribution on the electrochemical kinetics of spinel ferrites remains elusive.

Various chemical routes have been employed to fabricate spinel ferrites and composites with diverse morphologies and structures. Chen et al. synthesized $ZnFe_2O_4$ microspheres and nanoparticles using a solvothermal process and self-template synthesizing method, and studied the influence of morphology on electrochemical performance [21]. Lee et al. prepared $MgFe_2O_4/Fe_2O_3$ hollow microspheres composites *via* polyol reaction of ethylene glycol by the hydrothermal process with the aid of sucrose to improve specific capacity [22]. Li et al. encapsulated $CoFe_2O_4$ nanoparticles into porous N-doped carbon nanofiber membrane by electrospinning method to enhance lithium storage performance [23]. Among the fabrication techniques, electrospinning stands out as a simple and reliable technique for the preparation of MFe_2O_4 nanofibers with high porosity, which significantly facilitates lithium-ion diffusion. To date, various types of spinel ferrite nanofibers have been successfully synthesized using this technique, including normal spinel $ZnFe_2O_4$ fibers [24], mixed spinel $MgFe_2O_4$ fibers [25], and inverse spinel $CoFe_2O_4$ fibers [26]. When spinel ferrites are employed as the

* Corresponding authors.
E-mail addresses: rongshengcai@licp.cas.cn (R. Cai), yqwang@qdu.edu.cn (Y. Wang).
[1] These authors contributed to this work equally.

https://doi.org/10.1016/j.jelechem.2026.119870
Received 20 November 2025; Received in revised form 20 January 2026; Accepted 21 January 2026
Available online 22 January 2026

anodes of LIBs, the specific spinel type governs the insertion/extraction of lithium ions at the tetrahedral or octahedral sites within the lattice, thereby influencing the reaction mechanism of the battery. However, the correlation between spinel type and electrochemical kinetic behavior of spinel ferrites remains inadequately explored.

In this work, three spinel-ferrite nanofibers, including normal spinel $ZnFe_2O_4$, mixed spinel $MgFe_2O_4$ and inverse spinel $CoFe_2O_4$, were prepared *via* electrospinning. The influence of spinel structure on electrochemical kinetic behavior of three spinel ferrites was systematically investigated. As an anode for LIBs, the ZFO electrode demonstrates the highest initial discharge platform and superior lithium-ion transport capability.

2. Experimental

2.1. Materials

Polyacrylonitrile (PAN, average Mw. 150,000), Iron acetylacetonate [$Fe(acac)_3$, 99%], Zinc acetylacetonate [$Zn(acac)_2$, 99%], Magnesium acetylacetonate [$Mg(acac)_2$, 99%], Cobalt acetylacetonate [$Co(acac)_2$, 99%] and *N*, *N*-Dimethylformamide (DMF, 99.8%) were purchased from Sinopharm Chemical Reagent Co., Ltd..

2.2. Preparation of $ZnFe_2O_4$, $MgFe_2O_4$ and $CoFe_2O_4$ fibers

We dissolved PAN in DMF to achieve a solution concentration of 11 wt%. Subsequently, $Fe(acac)_3$ and $M(acac)_2$ (Zn, Mg, Co) with a molar ratio of 2:1 was dissolved in the aforementioned solution. An appropriate amount of spinning solution was drawn into a disposable syringe, and the spinning solutions were spun into nanofiber membranes using a single-needle electrospinning machine. The detailed parameters for the electrospinning process can be found in our previous work [13]. After spinning for 6 h, the resulting fiber membrane was dried at 25 °C for 2 h to remove the residual solvents. Finally, an annealing process was carried out at 800 °C with a heating rate of 2 °C/min in air to produce spinel-ferrite nanofibers. The fiber membranes derived from the three initial precursor solutions are labeled as ZFO (for $ZnFe_2O_4$), MFO (for $MgFe_2O_4$), and CFO (for $CoFe_2O_4$).

2.3. Materials characterization

X-ray diffraction (XRD) patterns were acquired on a SmartLab XRD diffractometer with Cu-K_α radiation ($\lambda = 1.5406$ Å). Scanning electron microscope (FE-SEM, Sigma 500) was used to characterize the morphology of the product at an accelerating voltage of 20 kV. Bright field (BF TEM) and high-resolution images (HRTEM) were obtained on conventional transmission electron microscope (JEOL JEM2010F) at an accelerating voltage of 200 kV. The high-angle annular dark field (HAADF) imaging and electron energy-loss spectroscopy (EELS) were carried out on spherical aberration-corrected scanning-transmission electron microscope (FEI Titan G280–200 STEM) at an accelerating voltage of 200 kV. An automatic volumetric sorption analyzer (NOVA 1100, Quantachrome, USA) was used to carry out nitrogen adsorption-desorption tests at 77 K. The Brunauer-Emmett-Teller (BET) and Barrett-Joyner-Halenda (BJH) method was used to determine the specific surface areas and the pore size distribution of the product, respectively.

2.4. Electrochemical measurements

ZFO, MFO and CFO materials were individually employed as active materials for the preparation of LIBs anodes. The detailed preparation procedure for the anodes and CR2025-type coin cells can be found elsewhere [10]. A LAND CT2001 battery testing system was used to examine the electrochemical performance with a voltage range from 0.01 V to 3.00 V at room temperature. The Metrohm Autolab electrochemical workstation (PGSTAT 302 N) was employed to perform the cyclic voltammetry (CV) measurements and electrochemical impedance spectroscopy (EIS) tests.

3. Results and discussion

The XRD patterns of the products are demonstrated in Fig. 1. The peaks of ZFO, MFO and CFO agree well with those of the standard card for cubic $ZnFe_2O_4$ (JCPDS no.: 22–1021, $a = 8.441$ Å), $MgFe_2O_4$ (JCPDS no.: 17–0464, $a = 8.375$ Å) and $CoFe_2O_4$ (JCPDS no.: 22–1086, $a = 8.392$ Å), respectively. This confirms the formation of pure $ZnFe_2O_4$, $MgFe_2O_4$ and $CoFe_2O_4$ at an annealing temperature of 800 °C in air. Careful observation shows that the arrangement of the main diffraction peaks is similar among these three products, although there are slight shifts in their positions [27,28]. This is attributed to the shared cubic crystal structure of ZFO, MFO and CFO, with the slight variations in lattice parameters resulting from differences in the ionic radius of Zn^{2+}, Mg^{2+} and Co^{2+}.

Fig. 2a, d and g display SEM images of the ZFO, MFO and CFO, respectively. It is observed that all three products exhibit uniform porous fiber morphology, with average sizes of 104 nm, 120 nm and 125 nm for ZFO, MFO, and CFO, respectively. Fig. 2b, e and h display TEM images of the three products. As observed from these images, all three products are nanofibers featuring a substantial number of surface pores, which is consistent with the SEM observations. Fig. 2c, f and i show HRTEM images of individual nanoparticles in the three nanofibers, respectively. The interplanar spacing in Fig. 2c is measured to be 2.98 Å, corresponding to the (220) plane of cubic ZFO. The interplanar spacing measured in Fig. 2f is 2.56 Å and 3.01 Å, corresponding to the $(3\bar{1}1)$ and (220) planes of MFO with a cubic structure. The interplanar spacing in Fig. 2i is determined to be 2.96 Å, consistent with the (220) plane of cubic CFO. From the above XRD and SEM analyses, it can be seen that ZFO, MFO and CFO nanofibers are composed of numerous nanoparticles.

STEM images were acquired to further explore the microstructure of different spinel ferrites. Fig. 3a, c and e show low-magnification STEM images of ZFO, MFO and CFO, respectively. Numerous pores occur on the surface of ZFO, MFO and CFO which can provide more lithium-storage sites and facilitate the transport of lithium ions [29]. Fig. 3b, d and F are HAADF images of individual nanoparticles in three nanofibers, respectively. The interplanar spacings measured in Fig. 3b are 2.56 Å and 3.01 Å, corresponding to the $(3\bar{1}1)$ and (220) planes of the cubic ZFO, respectively, with a plane angle of 62°. The measured planar spacing in Fig. 3d is 3.01 Å and 3.50 Å, corresponding to the (220) and $(1\bar{1}1)$ planes of the cubic MFO, with a plane angle of 90°. The plane spacings in Fig. 3f are measured to be 2.96 Å and 2.55 Å, corresponding to the (220) and $(3\bar{1}1)$ planes of the CFO, with a plane angle of 65°. The above analyses further demonstrate that ZFO, MFO and CFO nanofibers are composed of nanoparticles.

The EELS spectra were thoroughly examined to investigate the variations in the electronic structure among the three different spinel-type ferrites. Since the overlap of the Mg-L_1 and Zn-$M_{2,3}$ peaks within the plasma loss region spanning from 30 to 100 eV, precise identification of the corresponding peak positions and shapes is challenging. Consequently, the high-energy loss peaks of ZFO and MFO only exhibit the Fe $L_{2,3}$ and O—*K* edge peaks, whereas the high-energy loss peaks of CFO display Co-$L_{2,3}$, Fe-$L_{2,3}$ and O—*K* edge peaks. As seen in Fig. 4a, c and e, for Fe-$L_{2,3}$ peaks, the gap between L_3 and L_2 peaks is 13.1 eV, and the intensity ratio (L_3/L_2) is 4.5, agreeing well with the reported results for $NiFe_2O_4$ [30]. This indicates that the valence states of Fe in ZFO, MFO and CFO nanofibers are all trivalent. Although no significant differences are observed in the fine structure of the Fe-$L_{2,3}$ edges across the three spinel-type ferrites, notable variations are present in the O—*K* edge peaks. As shown in Fig. 4b, d, and f, the O—*K* edge exhibits a distinct splitting into three peaks, which is related to crystal-field cleavage and

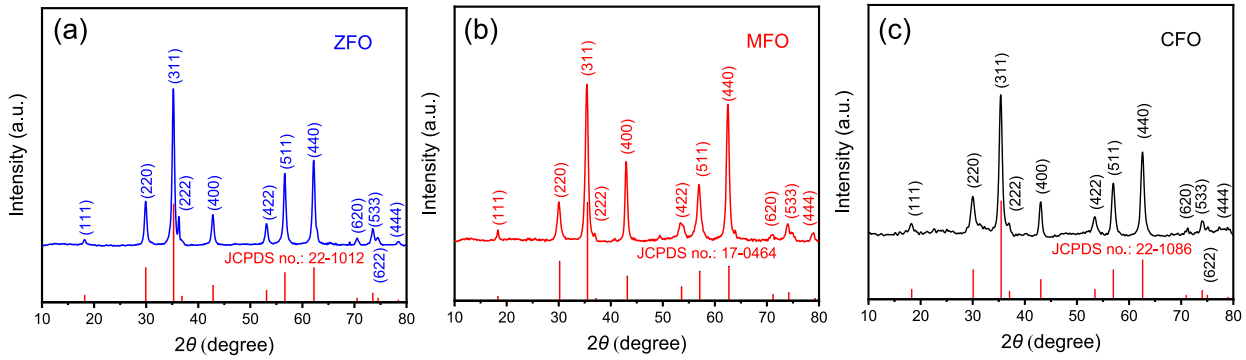

Fig. 1. XRD patterns of ZFO (a), MFO (b) and CFO (c).

lattice distortion, resulting from the hybridization of O 2*p* and metal 3*d* orbitals [31]. Careful observation shows that the positions and intensities of the peak *B* are nearly identical. However, significant differences are observed in both the positions and intensities of the peak *A* among these samples. Specifically, there is a significant shift in the position of peak *A*: 531.3 eV for ZFO, 530.8 eV for MFO and 529.8 eV for CFO. Moreover, the intensity ratios of peak *A* to peak *B* for ZFO, MFO, and CFO are 0.27, 0.29, and 0.35, respectively. This suggests that the degree of hybridization between the O 2*p* orbitals and metal 3*d* orbitals increases sequentially in ZFO, MFO, and CFO. This finding is consistent with previously reported results [32] and further confirms that ZFO, MFO, and CFO possess different types of spinel structures. Our theoretical calculations [17] show that the degree of hybridization between the O 2*p* orbitals and Fe 3*d* orbitals is lowest in ZFO and largest in CFO, consistent with the EELS results.

XPS spectra were acquired to further investigate the elemental valence states of Zn, Mg, Co and Fe in the three spinel ferrites. Fig. 5a displays the XPS spectrum of Zn 2*p* obtained from the ZFO. The peaks at 1021.3 eV and 1044.4 eV can correspond to Zn $2p_{3/2}$ and Zn $2p_{1/2}$ of Zn^{2+} [33], respectively, indicating that the Zn element in the ZFO has a valence of +2. Fig. 5b presents the Fe 2*p* spectrum acquired from the ZFO, where the peaks at 724.4 eV and 711.3 eV are assigned to Fe $2p_{1/2}$ and Fe $2p_{3/2}$ of Fe^{3+} located in the octahedral sites of the spinel structure [12], confirming that ZFO possesses normal spinel structure. The additional peaks observed are satellite peaks from Fe^{3+}. For MFO, Fig. 5c displays the Mg 1 *s* spectrum, where the peak at 1303.7 eV corresponds to Mg^{2+}, indicating that the Mg element in MFO exists as Mg^{2+} [34]. Further, the Mg 1 *s* peak at 1303.7 eV is deconvoluted into two peaks located at 1303.0 and 1304.6 eV, corresponding to Mg^{2+} in the tetrahedral and octahedral sites of the spinel structure, respectively [35]. In accordance with integrated intensity of deconvoluted peaks, the distribution of Mg^{2+} is 88.7% at tetrahedral sites and 11.3% at octahedral sites [17]. Fig. 5d illustrates the Fe 2*p* spectrum in MFO, where the peaks at 724.9 eV and 711.3 eV correspond to Fe $2p_{1/2}$ and Fe $2p_{3/2}$ of Fe^{3+}. Furthermore, two peaks situated at 713.3 and 710.0 eV can be deconvoluted from the Fe $2p_{3/2}$ peak at 711.3 eV, while two peaks at 727.4 and 724.8 eV can be deconvoluted from the Fe $2p_{1/2}$ peak at 724.9 eV, which are assigned to Fe^{3+} ions that occupy the tetrahedral and octahedral sites, respectively, within the spinel structure [35]. In accordance with the integrated intensity of deconvoluted peaks, the distribution of Fe^{3+} is determined to be 11.6% at tetrahedral sites and 88.4% at octahedral sites [12], confirming that MFO adopts a mixed spinel structure. Similarly, for CFO, Fig. 5e shows the XPS spectrum of Co 2*p*. The peaks at 779.8 eV and 795.6 eV correspond to Co $2p_{3/2}$ and Co $2p_{1/2}$ of Co^{2+}, indicating that the Co element in CFO exists in the form of Co^{2+} [36]. The Fe 2*p* spectrum in Fig. 5f also shows that the peaks at 724.8 eV and 711.1 eV are consistent with Fe $2p_{1/2}$ and Fe $2p_{3/2}$ of Fe^{3+}. The Fe $2p_{3/2}$ peak at 711.1 eV is deconvoluted into two peaks at 711.9 and 710.6 eV, and the Fe $2p_{1/2}$ peak at 724.8 eV is deconvoluted into two peaks at 725.7 and 724.1 eV. These two peaks correspond to Fe^{3+} ions residing at tetrahedral and octahedral sites within the spinel structure [37], consistent with the findings observed in ZFO and MFO. According to the integrated intensity of deconvoluted peaks, the distribution of Fe^{3+} is calculated to be 50.1% at tetrahedral sites and 49.9% at octahedral sites [12], confirming that CFO exhibits an inverse spinel structure.

Nitrogen adsorption-desorption tests were undertaken to evaluate the specific surface area. It can be seen from Fig. 6a that the physical isotherms of all samples are type IV, indicating that ZFO, MFO and CFO have mesoporous structures. The distribution curves for the pore size in Fig. 6b indicate that the predominant average pore sizes for ZFO, MFO and CFO are 24.4 nm, 23.7 nm and 21.3 nm, respectively. The specific surface areas calculated for ZFO, MFO and CFO are 39.4, 30.9 and 26.1 $m^2\ g^{-1}$, respectively. The BET test results, as summarized in Table 1, indicate that ZFO exhibits the largest specific surface area, although the pore sizes of the three spinel types are comparable. The increased specific surface area can enhance the transport of Li^+ ions and facilitate their diffusion within the electrode. In addition, it ensures that the electrode and the electrolyte keep an effective contact, thus providing more active sites for the Li^+-ion storage.

The electrochemical reaction process was investigated through the CV test. Fig. 7a, c and e show CV curves for the first five cycles of ZFO, MFO and CFO electrodes, respectively. For the first cycle of the cathodic scan, the reduction peak of the ZFO electrode at 1.48 V corresponds to the insertion of Li^+ ions [37]. The reduction peak at 0.52 V is related to the reduction of Zn^{2+} and Fe^{3+} to Zn^0 and Fe^0, including the formation of the solid electrolyte interface (SEI) film on the surface of the anode material, and the Li—Zn alloying reaction [38], which is shown in Eq. (1) and Eq. (2). For the first cycle of the anodic scan, the oxidation peak of the ZFO electrode at 1.70 V corresponds to the oxidation of Zn^0 and Fe^0 into Zn^{2+} and Fe^{3+} [39], and the electrochemical reactions are shown in Eq. (3) and Eq. (4). The electrochemical reactions are listed as follows [40–42].

$$ZnFe_2O_4 + 8Li^+ + 8e^- \rightarrow Zn + 2Fe + 4Li_2O \quad (1)$$

$$Zn + Li^+ + e^- \rightarrow LiZn \quad (2)$$

$$Zn + Li_2O \rightarrow ZnO + 2Li^+ + 2e^- \quad (3)$$

$$2Fe + 3Li_2O \rightarrow Fe_2O_3 + 6Li^+ + 6e^- \quad (4)$$

For the first cycle of the cathode scan, the reduction peak of the MFO electrode at 1.48 V is related to the insertion of Li^+ ions. The reduction peak at 0.49 V results from the reduction of Fe^{3+} to Fe^0 (dispersed in the amorphous Li_2O) and the formation of MgO, and the electrochemical reaction is demonstrated in Eq. (5). In this process, the structure of MFO undergoes irreversible destruction, and the resulting iron nanoparticles are inserted in amorphous MgO and Li_2O matrices [43,44]. The reduction peak at 0.17 V is ascribed to the formation of the SEI film [45]. For the first cycle of the anodic sweep, the oxidation peak of the MFO electrode at 1.65 V refers to the oxidation of Fe^0 to Fe_2O_3 [46–48], and

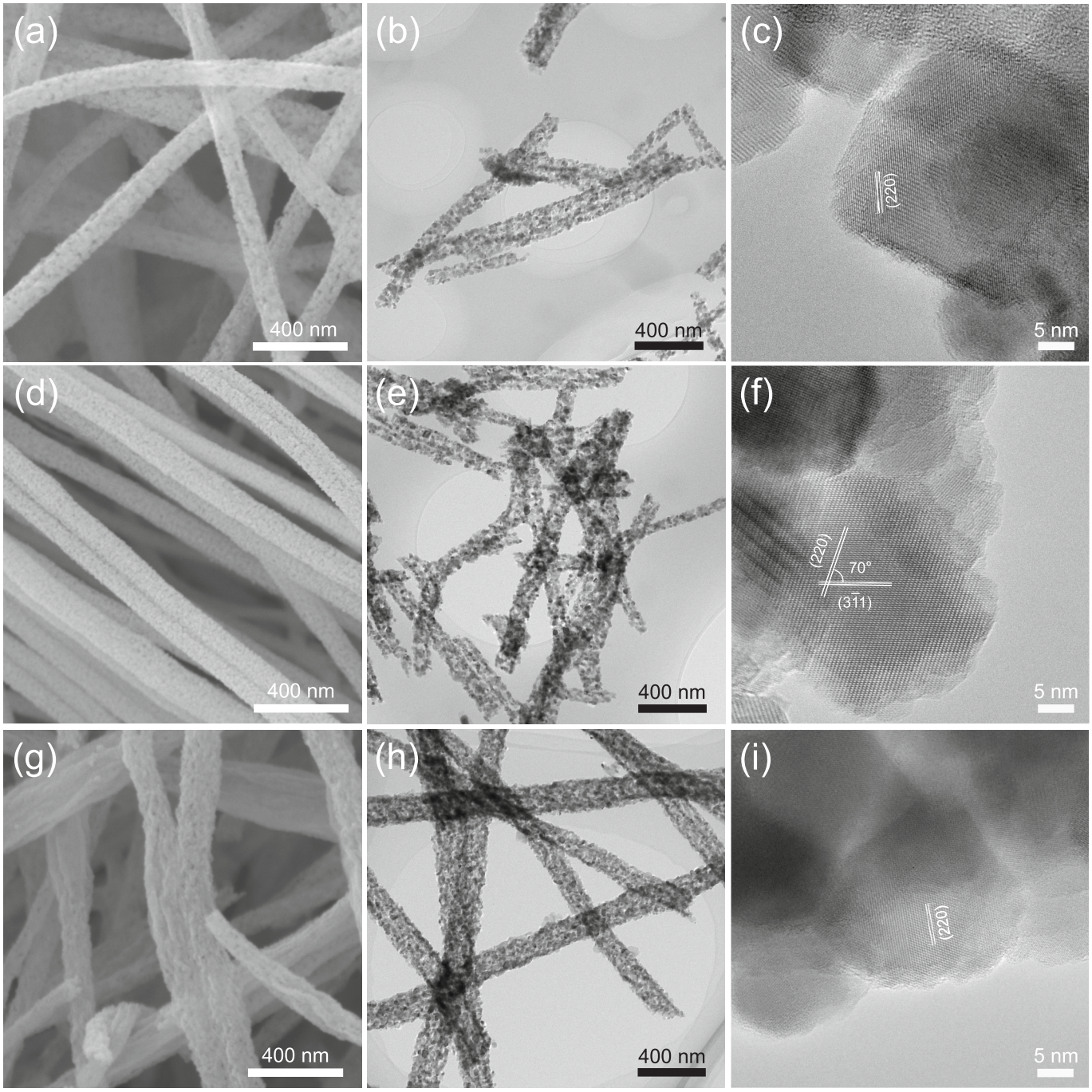

Fig. 2. SEM images of ZFO (a), MFO (d) and CFO (g), TEM and HRTEM images of ZFO (b, c), MFO (e, f) and CFO (h, i).

the electrochemical reaction is shown in Eq. (6). MgO is not involved in this reversible reaction because of its poor electrochemical activity. As a useful dispersant, MgO prevents the aggregation of iron nanoparticles, mitigating volume changes in the electrochemical processes [49]. The above electrochemical reaction is described as follows [43,44,49].

$$MgFe_2O_4 + 6Li^+ + 6e^- \rightarrow MgO + 2Fe + 3Li_2O \quad (5)$$

$$2Fe + 3Li_2O \rightarrow Fe_2O_3 + 6Li^+ + 6e^- \quad (6)$$

For the first cycle of the cathodic scan, the reduction peak of the CFO electrode at 0.48 V refers to the reduction of Fe^{3+} and Co^{2+} to Fe^0 and Co^0, the formation of Li_2O and SEI films [50,51], and the electrochemical reaction is shown in Eq. (7). For the first cycle of the anodic sweep, the oxidation peak of the CFO electrode at 1.77 V is attributed to the oxidation of Co^0 and Fe^0 into Co^{2+} and Fe^{3+} [52,53], and the electrochemical reactions are shown in Eq. (8) and Eq. (9). The above electrochemical reactions are summarized as follows.

$$CoFe_2O_4 + 8Li^+ + 8e^- \rightarrow Co + 2Fe + 4Li_2O \quad (7)$$

$$Co + Li_2O \rightarrow CoO + 2Li^+ + 2e^- \quad (8)$$

$$2Fe + 3Li_2O \rightarrow Fe_2O_3 + 6Li^+ + 6e^- \quad (9)$$

Unlike the first cycle, the peaks of the second to five cycles of the ZFO electrode are basically the same, indicating that the anode active material undergoes structural reconstruction in the first cycle. The change in the redox peak arises from the formation of the SEI film and the transformation reaction [54,55]. The overlapping peaks in the second to

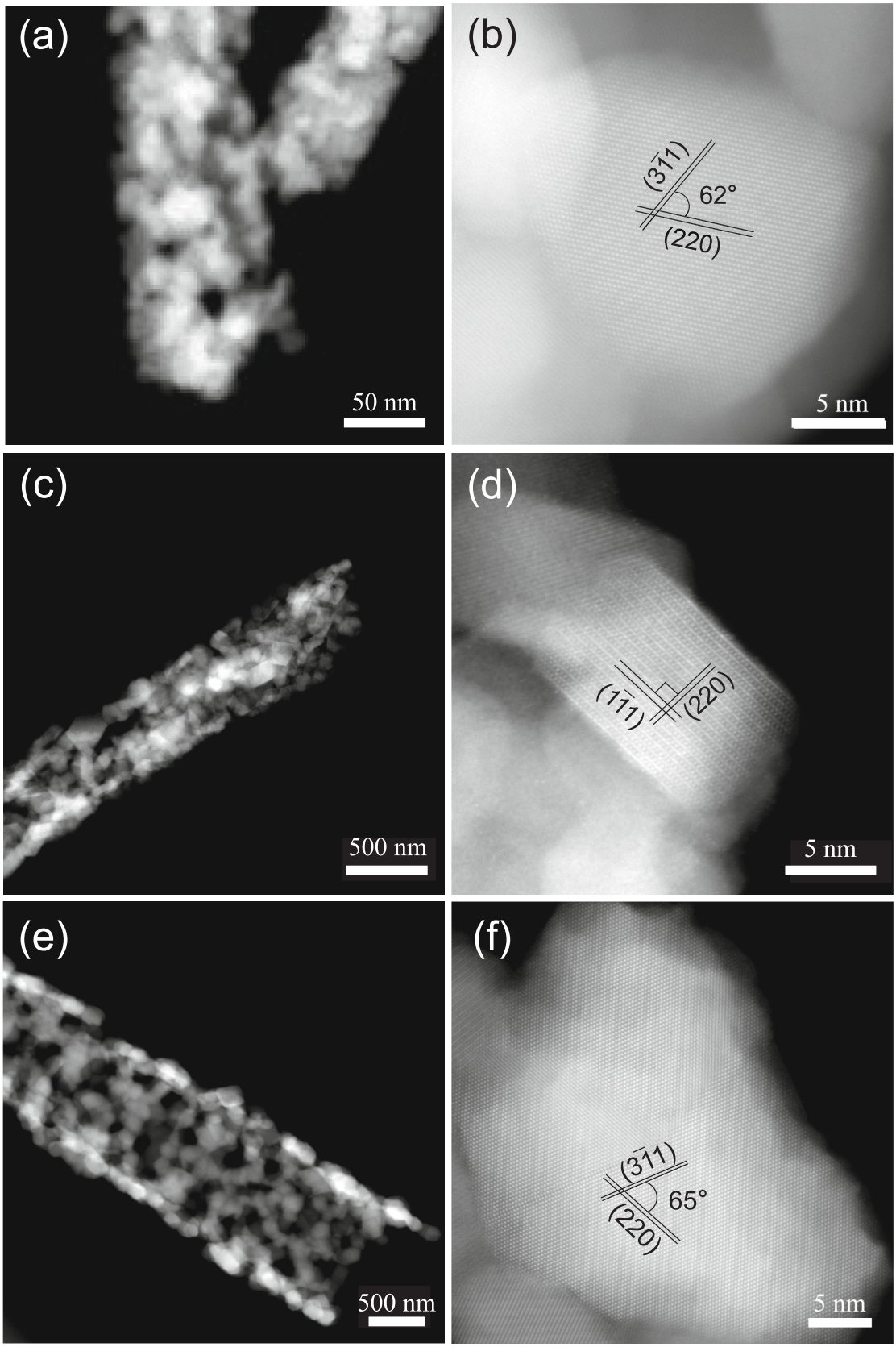

Fig. 3. STEM and HAADF images of ZFO (a, b), MFO (c, d) and CFO (e, f).

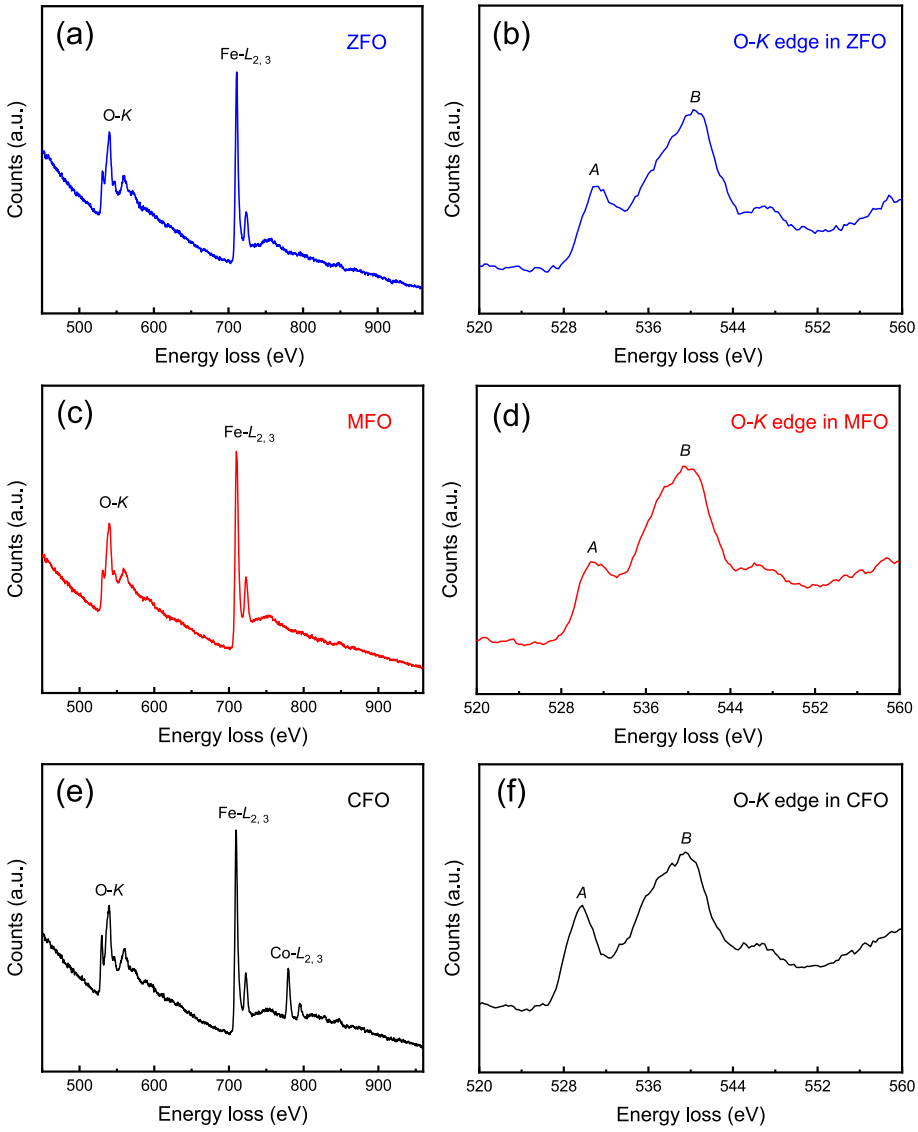

Fig. 4. EELS spectra of ZFO (a), MFO (c) and CFO (e), O—*K* edges in ZFO (b), MFO (d) and CFO (f).

five cycles suggest that the electrochemical process of the MFO electrode is highly reversible, and the change in redox peaks is ascribed to the formation of the SEI film and the transformation reaction of the active material [44,56]. Similarly, the CFO electrode undergoes structural reconstruction during the first cycle, with the change in redox peaks attributed to the formation and transformation of the SEI film [52,53].

Representative voltage profiles of the first cycle *versus* number of electron equivalents are plotted in Fig. 8. The theoretical number of electrons discharged for ZFO and CFO is eight, corresponding to full reduction of Fe^{3+} and Zn^{2+} into Fe^0 and Zn^0 [Eq. (1) and (7)]. MFO only delivers six electrons upon full lithiation because of electrochemical inactivity of formed MgO [Eq. (5)]. From Fig. 8a, it can be seen that all three electrodes demonstrate a short platform and a long platform. The short platform corresponds to initial insertion of Li^+ ion into the interstitial octahedral sites of the spinel structure, while the long platform is related to conversion reaction [57,58]. To show the differences of short platforms for the first discharge cycle of three spinel ferrites more clearly, the enlarged profiles of voltage *vs.* electron equivalent are displayed in Fig. 8b. For ZFO, the first discharge voltage platform is observed at 1.5 V, higher than those of MFO (1.4 V) and CFO (1.3 V). This is closely related to the octahedral site occupancy percentage in the three spinels. According to XPS results, the percentages of iron ions occupying the octahedral sites in the ZFO, MFO and CFO are 100%, 88.7% and 50.1% respectively. Thus, it is deduced that the larger octahedral site occupancy percentage, the higher discharge voltage platform. Moreover, in the spinel structure, the octahedral site is larger than tetrahedral site, and octahedral site has lower energy than tetrahedral site. Therefore, lithium ions can be more easily inserted into the octahedral site than the tetrahedral site. From the above analysis, it is concluded that the greater the proportion of iron ions that occupy the octahedral sites in the spinel structure, the easier for the lithium ions to be inserted into the anodes.

Fig. S1a displays the cycling performance of ZFO, MFO and CFO electrodes at a current density of 0.1 A g^{-1}. ZFO electrode retains a discharge capacity of 412.4 mAh g^{-1} after 100 cycles, while for MFO and CFO electrodes, the discharge capacity decreases to 296.8 and 182.8 mAh g^{-1} after 100 cycles, respectively. ZFO electrode exhibits the best cycling performance, which is mainly ascribed to the fact that ZFO has the largest specific surface area, providing more space for the storage of lithium ions. The initial Coulombic efficiency of the ZFO electrode is 83%, and reaches 99% in subsequent cycles. Rate capability was assessed at various current densities, as depicted in Fig. S1b. ZFO demonstrates average discharge capacities of 879.9, 414.2, 225.7, 129.0, and 56.4 mAh g^{-1} at 0.1, 0.2, 0.5, 1.0, and 2.0 A g^{-1},

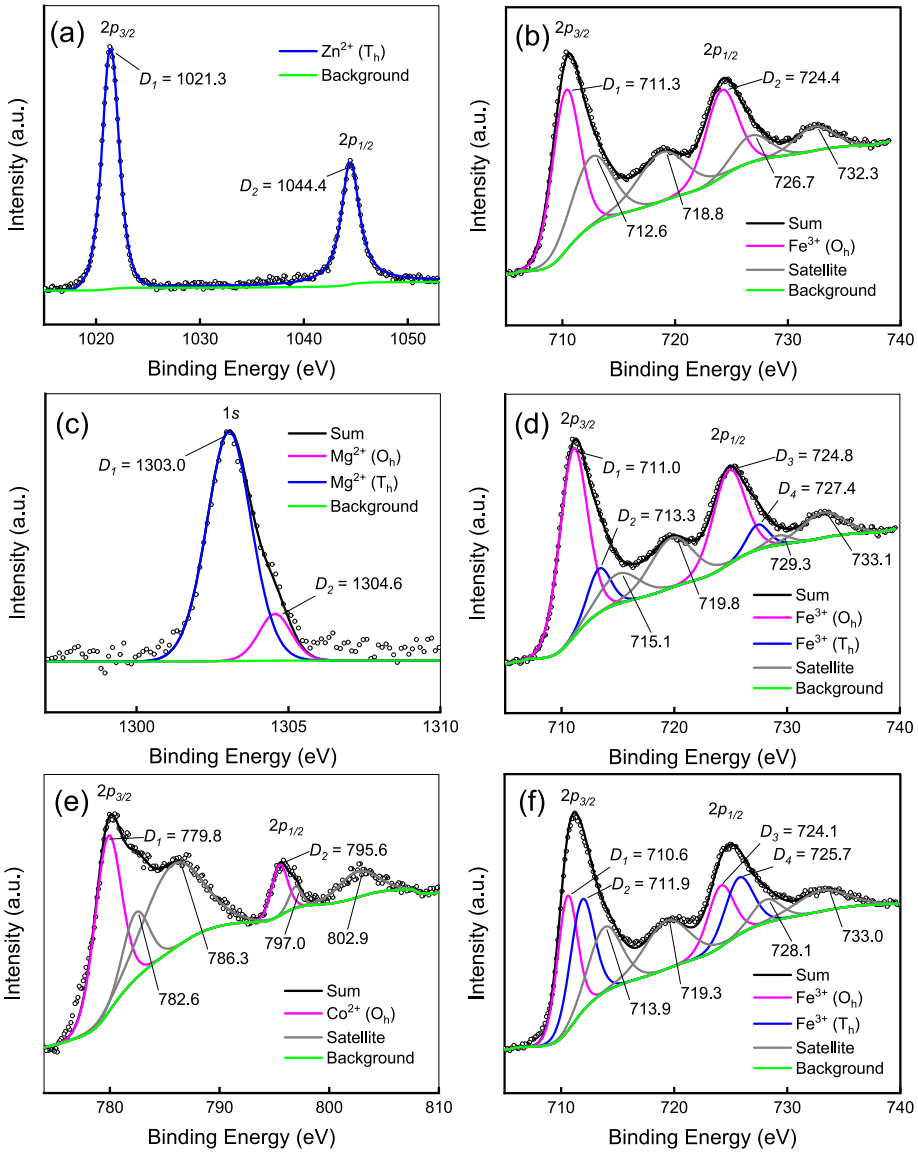

Fig. 5. XPS spectra of Zn 2*p* (a) and Fe 2*p* (b) for ZFO, XPS spectra of Mg 1 *s* (c) and Fe 2*p* (d) for MFO, XPS spectra of Co 2*p* (e) and Fe 2*p* (f) for CFO.

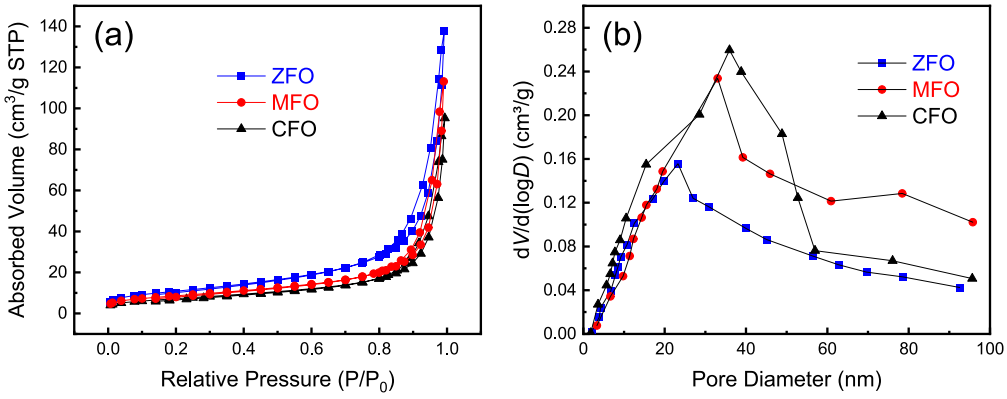

Fig. 6. Nitrogen adsorption/desorption isotherms (a) and pore size distribution curves (b) of ZFO, MFO and CFO.

respectively. Compared to MFO and CFO, the average discharge of ZFO is higher at the same current density, indicating a better rate capability. When the current density returns to 0.1 A g^{-1}, the capacity of ZFO reaches 458.1 mAh g^{-1}, surpassing that of the MFO (243.2 mAh g^{-1}) and CFO (222.6 mAh g^{-1}).

EIS test was performed to further investigate the electrochemical reaction kinetics of ZFO, MFO and CFO electrodes. Fig. 9a presents the EIS spectra and the corresponding equivalent circuit diagrams for the

Table 1
BET test results of ZFO, MFO and CFO.

Spinel	Specific surface area ($m^2\ g^{-1}$)	Average pore size (nm)
ZFO	39.4	24.4
MFO	30.9	23.7
CFO	26.1	21.3

three electrodes, where R_s, R_{ct}, W and CPE represent the electrolyte resistance, charge transfer resistance, Warburg impedance and constant phase element, respectively [59]. EIS spectra consist of a semi-circle and an inclined line in the high-frequency and low-frequency regions, respectively [60]. The diameter of the semi-circle is the smallest for the ZFO electrode, indicating that ZFO has the lowest charge transfer impedance. Furthermore, the slope of the inclined line at the low frequency region is associated with the diffusion of lithium ions. The diffusion coefficient, D_{Li}, can be determined using the formula as follows.

$$D_{Li} = \frac{R^2T^2}{2A^2n^4F^4C^2\sigma^2} \tag{10}$$

$$C = \frac{n}{V} = \frac{m/M}{V} \tag{11}$$

$$Z_{re} = R_s + R_{ct} + \sigma\omega^{-0.5} \tag{12}$$

where F is 96,485C mol^{-1} and R is 8.314 $J\ K^{-1}\ mol^{-1}$. A stands for the area of the electrode (1.54 cm^2), n refers to the number of electrons per molecule which is involved in the electron transfer reaction, T is 298.15 K, and C is calculated to be 2.21×10^4 mol m^{-3} (ZFO), 1.70×10^4 mol m^{-3} (MFO) and 2.25×10^4 mol m^{-3} (CFO) from formula (11). Fig. 9b displays the line plot between Z_{re} and $\omega^{-0.5}$. The σ values of ZFO,

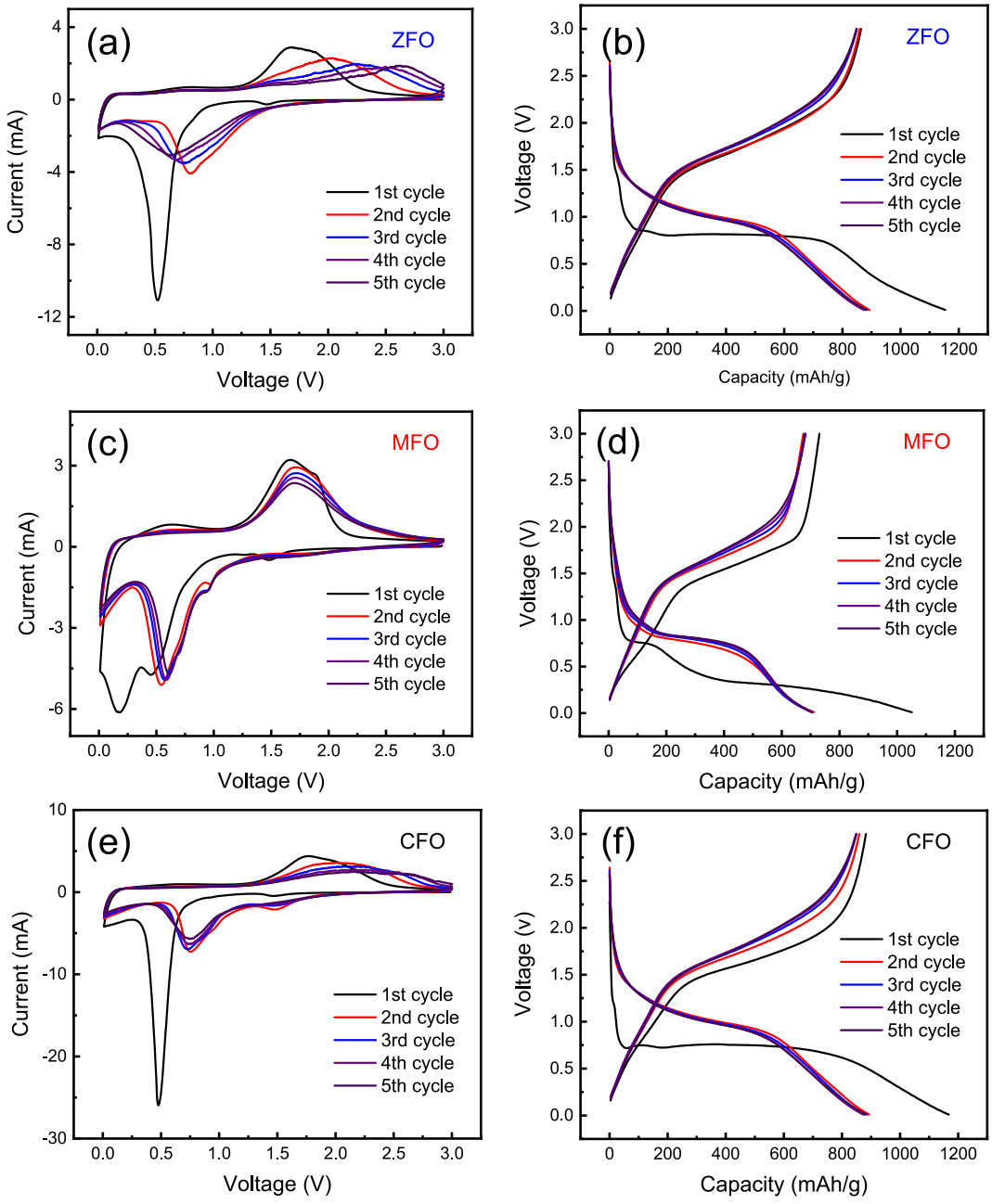

Fig. 7. CV curves of the first five cycles at 0.3 mV s^{-1} for ZFO (a), MFO (c) and CFO (e), the charge-discharge curves of the first five cycles at 0.2 A g^{-1} for ZFO (b), MFO (d) and CFO (f).

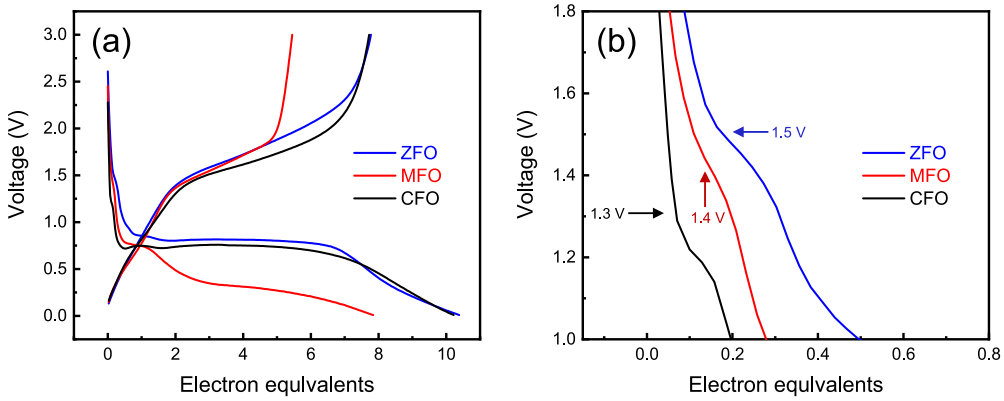

Fig. 8. (a) Representative voltage *vs.* electron equivalent profiles for the first cycle of ZFO, MFO and CFO electrodes at 0.2 A g^{-1} in the voltage range of 0.01 to 3.0 V, (b) The enlarged voltage *vs.* electron equivalent profiles for first discharge cycle of ZFO, MFO and CFO.

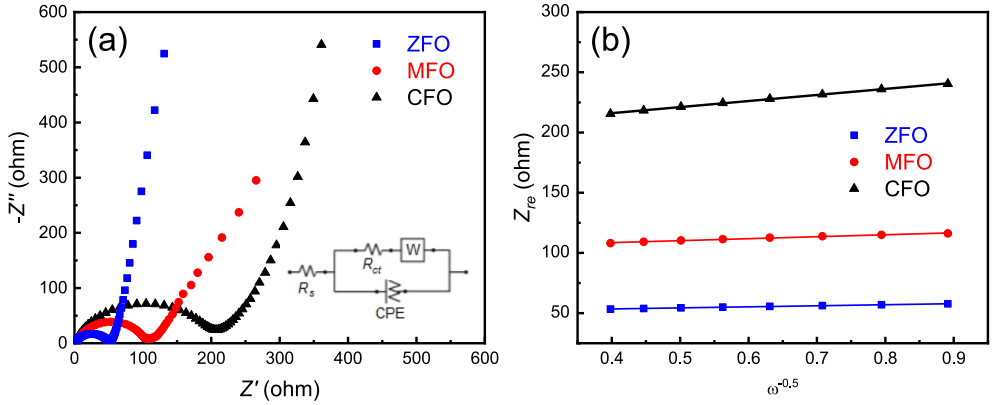

Fig. 9. EIS spectra (a) and line plot between Z_{re} and $\omega^{-0.5}$ (b) of ZFO, MFO and CFO electrodes.

MFO and CFO electrodes are determined to be 8.8, 16.3 and 50.4 Ω $s^{-0.5}$, respectively. The Li^+ diffusion coefficients of ZFO, MFO and CFO electrodes are calculated to be 3.95×10^{-17}, 1.95×10^{-17} and 1.16×10^{-17} cm^2 s^{-1}, respectively, demonstrating that ZFO electrode has the best ion-diffusion ability. This result indicates that Fe^{3+} in the ZFO, all located in the active centers of the octahedral sites, can help to promote charge transfer and diffusion of Li^+ ions.

To elucidate the electrochemical process more clearly, both ZFO and CFO electrodes (after 5 discharge cycles at 0.1 A g^{-1}) were characterized by TEM, as shown in Fig. S2 and S3. It can be seen from Fig. S2a and S3a that both ZFO and CFO maintain the fibrous morphology. The lattice spacings in Fig. S2c and S2d are measured to be 2.03 Å and 2.47 Å, corresponding to (110) plane of Fe (JCPDS no.: 06–0696) and (002) plane of Zn (JCPDS no.: 04–0831), respectively. The lattice spacings in Fig. S3c and S3d are measured to be 2.03 Å and 2.17 Å, consistent with (110) plane of Fe (JCPDS no.: 06–0696) and (100) plane of Co (JCPDS no.: 05–0727), respectively. These results indicate the Zn and Fe nanoparticles form after 5 cycles of ZFO electrode, while Co and Fe nanoparticles are produced after 5 cycles of CFO electrode, as supported by the CV curves in Fig. 7a and e.

4. Conclusions and future perspectives

In summary, ferrite fibers of different spinel types, including normal spinel ZFO, mixed spinel MFO and inverse spinel CFO, were prepared by electrospinning technique, and used as anode materials in LIBs. It is found that the initial Li^+ insertion potential increases with the octahedral site occupancy of Fe^{3+} in the spinel. Normal spinel ZFO exhibits the highest initial discharge voltage platform. This is mainly attributed to the large proportion of Fe^{3+} occupying octahedral position in normal spinel structure, which is conducive to promoting the diffusion ability of Li^+ ions into the lattice of the anode. The superior cycling performance and rate capability of ZFO are ascribed to the fiber morphology and large specific surface area, which offers more space for Li^+ storage, thereby enhancing lithium storage capacity. The findings of this work provide significant insights into the effect of spinel structure on the electrochemical behavior of spinel ferrites, highlighting the importance of structural design in optimizing battery performance. Future research will focus on optimizing synthesis methods, exploring doping strategies, developing composite materials. The elaborate design and synthesis of tailored spinel ferrites with optimized structural and electrochemical characteristics will be pivotal in advancing the performance and scalability of LIBs for next-generation energy storage technologies.

CRediT authorship contribution statement

Meng Sun: Writing – original draft, Investigation, Formal analysis. **Guanting Liu:** Investigation, Formal analysis. **Shujin Hao:** Writing – review & editing, Formal analysis. **Feiyu Diao:** Writing – review & editing. **Federico Rosei:** Writing – review & editing. **Rongsheng Cai:** Validation, Data curation. **Yiqian Wang:** Writing – review & editing, Supervision, Funding acquisition, Conceptualization.

Declaration of competing interest

The authors declare that they have no known competing financial interests or personal relationships that could have appeared to influence the work reported in this paper.

Acknowledgments

The authors gratefully acknowledge the financial support from the High-end Foreign Experts Programs, China (Grant Nos.: G2022025015L, G2022025016L, H20250033), and Shandong Province "Double-Hundred Talent Plan" Program (Grant No.: WST2018006). Y. Q. Wang acknowledges the support from the Taishan Scholar Program of Shandong Province, China, the Qingdao International Center of Semiconductor Photoelectric Nanomaterials, and the Shandong Provincial University Key Laboratory of Optoelectrical Material Physics and Devices.

Appendix A. Supplementary data

Supplementary data to this article can be found online at https://doi.org/10.1016/j.jelechem.2026.119870.

References

[1] A. Paolella, W. Zhu, G. Bertoni, S. Savoie, Z.M. Feng, H. Demers, V. Gariepy, G. Girard, E. Rivard, N. Delaporte, A. Guerfi, H. Lorrmann, C. George, K. Zaghib, Discovering the influence of lithium loss on garnet Li7La3Zr2O12 electrolyte phase stability, ACS Appl. Energy Mater. 3 (2020) 3415–3424.

[2] S.A. Mirshokraee, M. Muhyuddin, R. Lorenzi, G. Tseberlidis, C. Lo Vecchio, V. Baglio, E. Berretti, A. Lavacchi, C. Santoro, Litchi-derived platinum group metal-free electrocatalysts for oxygen reduction reaction and hydrogen evolution reaction in alkaline media, SusMat 3 (2023) 248–262.

[3] O. Simoska, E.M. Gaffney, S.D. Minteer, A. Franzetti, P. Cristiani, M. Grattieri, C. Santoro, Recent trends and advances in microbial electrochemical sensing technologies: An overview, Curr. Opin. Electroche. 30 (2021) 100762.

[4] M.J. Wu, F. Dong, Y.K. Yang, X. Cui, X.Q. Liu, Y.H. Zhu, D.S. Li, S. Omanovic, S. H. Sun, G.X. Zhang, Emerging atomically precise metal nanoclusters and ultrasmall nanoparticles for efficient electrochemical energy catalysis: synthesis strategies and surface/interface engineering, Electrochem. Energy R. 7 (2024) (Article 10).

[5] L.S. Zhang, F. Xie, S.J. Hao, F.Y. Diao, Y.Q. Wang, Annealing condition engineering of electrospun iron-titanium oxide nanofibers for enhanced lithium storage performance, Electrochim. Acta 526 (2025) (Article 146746).

[6] S.J. Hao, B. Zhang, Q.Y. Zhang, M. Sun, R.S. Cai, F.Y. Diao, Y.Q. Wang, Effectiveness of three distinct strategies of constructing ZnO-based composites for enhanced electrochemical performance, J. Phys. Chem. Solid 211 (2026) (Article 113502).

[7] A. Paolella, G. Bertoni, W. Zhu, D. Campanella, A. La Monaca, G. Girard, H. Demers, A.C.G. Nita, Z.M. Feng, A. Vijh, A. Guerfi, M. Trudeau, M. Armand, S. A. Krachkovskiy, Unveiling the cation exchange reaction between the NASICON Li1.5Al0.5Ge1.5(PO4)3 solid electrolyte and the pyr13TFSI ionic liquid, J. Am. Chem. Soc. 144 (2022) 3442–3448.

[8] A. Paolella, W. Zhu, G. Bertoni, A. Perea, H. Demers, S. Savoie, G. Girard, N. Delaporte, A. Guerfi, M. Rumpel, H. Lorrmann, G.P. Demopoulos, K. Zaghib, Toward an all-ceramic cathode-electrolyte interface with low-temperature pressed NASICON Li1.5Al0.5Ge1.5(PO4)3 electrolyte, Adv. Mater. Interfaces 7 (2020) (Article 2000164).

[9] W.F. Li, M.J. Xiao, J.T. Jiang, Y.Q. Li, X. Zhang, S.M. Li, X.M. Lin, D.L. Peng, S. W. Or, S.H. Sun, Z.Y. Xing, Co4N nanoparticles embedded in N-doped carbon pores: advanced interlayer material for lithium-sulfur batteries, Nano Energy 142 (2025) (Article 111140).

[10] M. Sun, X.L. Sheng, Z.P. Cui, S.J. Li, Q.Y. Zhang, F. Xie, G.T. Liu, S.J. Hao, F. Y. Diao, S.D. Sun, Y.Q. Wang, Complexant-facilitated assembly of NiTiO3 nanoparticles into microbars for high-performance lithium-ion battery anode, J. Am. Ceram. Soc. 107 (2024) 8650–8660.

[11] J.P. Qu, Y.S. Zhao, Y.R. Ji, Y.R. Zhu, T.F. Yi, Approaching high-performance lithium storage materials by constructing Li2ZnTi3O8@LiAlO2 composites, Int. J. Min. Met. Mater. 30 (2023) 611–620.

[12] L.W. Ji, O. Toprakci, M. Alcoutlabi, Y.F. Yao, Y. Li, S. Zhang, B.K. Guo, Z. Lin, X. W. Zhang, Λ-Fe2O3 nanoparticle-loaded carbon nanofibers as stable and high-capacity anodes for rechargeable lithium-ion batteries, ACS Appl. Mater. Interfaces 4 (2012) 2672–2679.

[13] X.L. Sheng, T. Li, M. Sun, G.J. Liu, Q.Y. Zhang, Z.B. Ling, S.W. Gao, F.Y. Diao, J. Z. Zhang, F. Rosei, Y.Q. Wang, Flexible electrospun iron compounds/carbon fibers: phase transformation and electrochemical properties, Electrochim. Acta 407 (2022) 139892.

[14] J.X. Xiao, X.S. Qi, X. Gong, Q. Peng, Y.L. Chen, R. Xie, W. Zhong, Tunable and improved microwave absorption of flower-like core@shell MFe2O4 @MoS2 (M = Mn, Ni and Zn) nanocomposites by defect and interface engineering, J. Mater. Sci. Technol. 139 (2023) 137–146.

[15] Q.Y. Yang, Y. Ma, Q.Y. Ye, Y.Q. Liu, Y.H. Luo, Y.B. Wu, Z.G. Xu, X.M. Lin, Prussian blue analogues derived MO/MFe2O4 (M = Ni, cu, Zn) nanoparticles as a high-performance anode material for enhanced lithium storage, Chin. J. Struct. Chem. 44 (2025) (Article 100631).

[16] L.S. Dong, Z.G. Wang, C. Mi, W.M. Zhao, C.L. Qin, C. Luo, Z.F. Wang, Defect-rich hierarchical porous spinel MFe2O4 (M = Ni, Co, Fe, Mn) as high-performance anode for lithium ion batteries, Mater. Today Chem. 35 (2024) 101853.

[17] G.T. Liu, J.J. Wang, X.L. Sheng, X.Y. Xue, Y.Q. Wang, Thermodynamics and electronic structure characteristics of MFe2O4 with different spinel structures: a first-principles study, Ceram. Int. 49 (2023) 29747–29754.

[18] J.Z. Ruan, Q. Cao, X.X. Li, Q.Y. Ren, M.L. Li, S.H. Dong, N.J. Li, Q.F. Xu, H. Li, J. M. Lu, D.Y. Chen, Morphology optimization of spinel catalysts for high-efficiency photothermal catalytic upcycling of polyethylene terephthalate, Adv. Mater. 37 (2025) (Article 2500090).

[19] Z. He, J.M. Liu, Y.Q. Wei, Y.F. Song, W.X. Yang, A.B. Yang, Y.X. Wang, B. Li, Polypyrrole-coated triple-layer yolk-shell Fe2O3 anode materials with their superior overall performance in lithium-ion batteries, Int. J. Min. Met. Mater. 31 (2024) 2737–2748.

[20] W.W. Wang, X. Yao, Z.C. Ma, J.L. Zhuo, Z.H. Lu, J.W. Sun, J.W. Cui, J.Q. Sha, NC coating MOF-derived CoFe2O4/C spinel for high performance lithium-ion batteries anode, Chem. Eng. J. 515 (2025) (Article 163912).

[21] C. Chen, J.C. Huang, J.G. Duh, Self-template fabrication of multi-scaled ZnFe2O4 microspheres and their excellent lithium-ion storage properties, J. Alloys Compd. 862 (2021) (Article 158342).

[22] S.B. Lee, R. Balasubramaniam, Double-shelled hybrid MgFe2O4/Fe2O3 hollow microspheres as a high-capacity anode for lithium-ion batteries, J. Ind. Eng. Chem. 110 (2022) 262–273.

[23] X.Q. Li, G.G. Guan, T.T. Zhao, J. Xiang, In-situ encapsulating ultrafine CoFe2O4 nanoparticle into porous N-doped carbon nanofiber membrane as self-standing anode for enhanced lithium storage performance, Electrochim. Acta 441 (2023) (Article 141787).

[24] X.K. Cui, Z.G. Zhu, M. Song, M. Li, J.W. Qi, Y.J. Zhou, Y. Yang, J.S. Li, ZnFe2O4-infused hierarchically porous carbon nanofiber electrode for enhanced capacitive deionization, Carbon 218 (2024) (Article 118761).

[25] W.F. Liu, Y.D. Pang, Z.P. Shi, H.Y. Yue, H.Y. Dong, Z.X. Cao, Z.X. Yang, S.T. Yang, Y.H. Yin, Ultrafast kinetics in a PAN/MgFe2O4 flexible free-standing anode induced by heterojunction and oxygen vacancies, ACS Appl. Mater. Interfaces 14 (2022) 11575–11586.

[26] X. Li, Y. Zhang, Z. Wang, H. Liu, J. Chen, Q. Yang, Advanced catalytic materials for energy conversion: a comprehensive review, Chem. Eng. J. 456 (2023) 148374.

[27] J.N. Baby, C. Lavanya, S.F. Wang, B. Sriram, A. Anantharaman, M. George, Sustainable synthesis of AFe2O4 (a = Mg, Zn, Mn) catalysts: comparing the photooxidative and electrochemical properties towards organic dyes detection and degradation, New J. Chem. 22 (2021) 10049–10056.

[28] H.T. Guo, X.T. Wang, H.J. Li, M.J. Liu, L.L. Xing, H.S. Zhai, AFe2O4 (A=Cu, Ni, Co, Mg, Ce, Mn) catalysts for hydrogen-rich syngas production from corn straw pyrolysis-catalytic steam reforming, Energ. Technol. 13 (2025) (Article 2401302).

[29] B. Yang, R.X. Pang, J.L. He, H. Sun, B.L. Yuan, M.Y. Zhang, Janus separator with high-temperature resistance and dendrite suppression for advanced Li-ions batteries, J. Power Sources 600 (2024) (Article 234259).

[30] J.J. Wang, X.L. Sheng, S.J. Hao, G.T. Liu, R.S. Cai, X.Y. Xue, Y.Q. Wang, Construction of Fe0.64Ni0.36@graphite nanoparticles via corrosion-like transformation from NiFe2O4 and surface graphitization in flexible carbon nanofibers to achieve strong wideband microwave absorption, J. Colloid Interface Sci. 657 (2024) 193–207.

[31] D. Takegami, K. Kawai, M.F. Carvalho, S. Rößler, C.E. Liu, C.Y. Kuo, C.F. Chang, A. Minamida, T. Miyazaki, M. Okubo, L.-H. Tjeng, T. Mizokawa, Valence study of Li(Ni0.5Mn0.5)1-xCoxO2 and LiNi1-xCoxO2: the role of charge transfer and charge disproportionation, Phys. Rev. Mater. 8 (2024) (Article 055401).

[32] J.N. Chen, Y.J. Qi, M. Lu, Y.M. Niu, B.S. Zhang, Identify fine microstructure of multifarious iron oxides via O K-edge EELS spectra, Chin. Chem. Lett. 33 (2022) 4375–4379.

[33] A.S. Chougale, S.S. Wagh, A.D. Waghmare, Boosting photoelectrochemical water splitting activity of zinc oxide by fabrication of ZnO/CdS heterostructure for hydrogen production, Adv. Compos. Hybrid Mater. 7 (2024) (Article 229).

[34] A. Padhan, P.M. Rajaitha, S. Nayak, S. Hajra, M. Sahu, Z. Jagličić, P. Koželj, H. Kim, Synthesis and application of mixed-spinel magnesioferrite: structural, vibrational, magnetic, and electrochemical sensing properties, Mater. Chem. Front. 7 (2023) 72–84.

[35] R.S. Yadav, I. Kuřitkal, J. Vilcakova, J. Havlica, J. Masilko, L. Kalina, J. Tkacz, J. Švec, V. Enev, M. Hajdúchová, Impact of grain size and structural changes on magnetic, dielectric, electrical, impedance and modulus spectroscopic characteristics of CoFe2O4 nanoparticles synthesized by honey mediated sol-gel combustion method, Adv. Nat. Sci. Nanosci. Nanotechnol. 8 (2017) (Article 045002).

[36] Y.N. Cao, W.W. Sun, C.F. Guo, L. Zheng, M.Y. Yao, Y. Wang, Rational construction of yolk-shell bimetal-modified quinonyl-rich covalent organic polymers with ultralong lithium-storage mechanism, ACS Nano 16 (2022) 9830–9842.

[37] J.M. Liu, Y.H. Lu, R.X. Wang, Z.F. Xu, X. Li, The effect of calcination temperature on combustion preparation of ZnFe2O4 as anode for lithium batteries, Int. J. Electrochem. Sci. 15 (2020) 1571–1580.

[38] Y.D. Ye, H.Y. Xie, Y.H. Yang, Y.S. Xie, Y.H. Lu, J.X. Wang, X.H. Kong, S. Jin, H.X. Ji, Solid-solution or intermetallic compounds: phase dependence of the Li-alloying reactions for Li-metal batteries, J. Am. Chem. Soc. 145 (2023) 24775–24784.

[39] Y.R. Lu, Y.F. Wang, H.W. Chang, Y.C. Huang, J.L. Chen, C.L. Chen, Y.C. Lin, Y.-G. Lin, W.-F. Pong, T. Ohigashi, N. Kosugi, C.-H. Kuo, W.-C. Chou, C.-L. Dong, Effect of Fe2O3 coating on ZnO nanowires in photoelectrochemical water splitting: a synchrotron X-ray spectroscopic and spectromicroscopic investigation, Sol. Energy Mater. Sol. Cells 209 (2020) (Article 110469).

[40] N. Tiwari, S. Kadam, R. Ingole, S. Kulkarni, Facile hydrothermal synthesis of ZnFe2O4 nanostructures for high-performance supercapacitor application, Ceram. Int. 48 (2022) 29478–29483.

[41] L. Wang, B.B. Li, H.Y. Bai, H. Ding, N. Xu, C.F. Yin, J.J. Xiong, Z.W. Yang, X.F. Rao, B.B. Dong, Preparation of nitrogen-doped ZnFe2O4-modified carbon composite and its collaborative energy storage mechanism, Coatings 13 (2023) (Article 1126).
[42] D. Spada, M. Ambrosetti, M.C. Mozzati, B. Albini, P. Galinetto, A. Cini, M. Fittipaldi, M. Bini, Understanding the electrochemical features of ZnFe2O4 anode for LIBs by deepening its physico-chemical properties, Mater. Res. Bull. 160 (2023) (Article 112132).
[43] S.Y. Lu, Z.H. Ding, H.M. He, Mg-Al hydroxide intercalated ionic liquids for quasi-solid-state lithium batteries, J. Solid State Electrochem. 27 (2023) 161–170.
[44] M. Latroche, D. Blanchard, F. Cuevas, A.E. Kharbachi, B.C. Hauback, T.R. Jensen, P.E. De Jongh, S. Kim, N.S. Nazer, P. Ngene, S. Orimo, D.B. Ravnsbæk, V.A. Yartys, Full-cell hydride-based solid-state Li batteries for energy storage, Int. J. Hydrogen Energy 44 (2019) 7875–7887.
[45] L. Luo, Z. Chen, H.Z. Ke, S. Sha, G.M. Cai, D.W. Li, H.J. Yang, X.W. Yang, R. Q. Zhang, J.Q. Li, Y.G. Li, J. Xu, W.L. Xu, Q.F. Wei, Facile synthesis of three-dimensional ZnFe2O4/graphene aerogel composites for high lithium storage performance and its application in full cell, Mater. Des. 182 (2019) (Article 108043).
[46] F. Xie, M. Sun, X.L. Sheng, Q.Y. Zhang, Z.B. Ling, S.J. Hao, F.Y. Diao, Y.Q. Wang, Graphene-wrapped Fe2TiO5 nanoparticles with enhanced performance as lithium-ion battery anode, Mater. Lett. 358 (2024) 135877.
[47] X. Yao, D. Li, L. Guo, M. Kallel, S.D. Alahmari, J. Ren, I. Seok, G. Roymahapatra, C. Wang, Carbon-coated LiMn0.8Fe0.2PO4 cathodes for high-rate lithium-ion batteries, Adv. Compos. Mater. 7 (2024) (63).
[48] X.B. Liu, M.X. Yu, S.G. Wu, J.B. Gong, Composite nanoarchitectonics for efficient lithium storage by encapsulating black phosphorus quantum dots in cobalt/iron based Prussian blue analogues, J. Alloys Compd. 969 (2023) (Article 172291).
[49] H. Park, H.K. Lim, S.H. Oh, J. Park, H.D. Lim, K. Kang, Tailoring ion-conducting interphases on magnesium metals for high-efficiency rechargeable magnesium metal batteries, ACS Energy Lett. 5 (2020) 3733–3740.
[50] Y. Wang, X.D. Guo, C.T. Chen, Y.S. Wang, Q. Li, Z.G. Wu, B.H. Zhong, Y.X. Chen, Alleviating the shuttle effect via bifunctional MnFe2O4/AB modified separator for high performance lithium sulfur battery, Electrochim. Acta 354 (2020) 136704.
[51] V.A. Jundale, A.A. Yadav, Electrochemical properties of CoFe2O4 thin film electrodes prepared by spray pyrolysis, Thin Solid Films 772 (2023) 139821.
[52] C.H. Yeh, W.Y. Hsu, C.C. Hsu, J.A.A. Valinton, C.I. Yang, C.C. Chiu, C.H. Chen, Cobalt iron oxides prepared by acidic redox-assisted precipitation: characterization, applications, and new opportunities, ACS Appl. Mater. Interfaces 13 (2021) 52181–52192.
[53] F.E. Farghaly, A.Y. Shenouda, Electrochemical behavior of negative electrode from co(OH)2 and graphene for lithium batteries, J. Mater. Sci. Mater. Electron. 32 (2021) 16139–16152.
[54] S.J. Hao, X.L. Sheng, F. Xie, M. Sun, F.Y. Diao, Y.Q. Wang, Electrospun carbon nanofibers embedded with heterostructured NiFe2O4/Fe0.64Ni0.36 nanoparticles as an anode for high-performance lithium-ion battery, J. Energy Storage 80 (2024) (Article 110412).
[55] J. Ryu, J. Park, W.G. Lim, J. Hwang, Unraveling the impact of pore length on the conversion reaction of Fe3O4/carbon anodes in lithium-ion batteries, Appl. Surf. Sci. 675 (2024) (Article 160976).
[56] J.M. Pan, D.M. Gao, Y.P. Liu, M. Nie, B. Shang, C.G. Chen, J.F. Wang, G.S. Huang, D.F. Zhang, F.S. Pan, NiAs-type vanadium sulfides: topological surface and abundant electroactivity as a bi-functional material in Mg/Li batteries, Appl. Surf. Sci. 645 (2024) (Article 158888).
[57] W. Zhang, D.C. Bock, C.J. Pelliccione, Y. Li, L. Wu, Y. Zhu, A.C. Marschilok, E. S. Takeuchi, K.J. Takeuchi, F. Wang, Insights into ionic transport and structural changes in magnetite during multiple-electron transfer reactions, Adv. Energy Mater. 6 (2016), 1502471.
[58] Y.N. NuLi, Y.Q. Chu, Q.Z. Qin, Nanocrystalline ZnFe2O4 and ag-doped ZnFe2O4 films used as new anode materials for Li-ion batteries, J. Electrochem. Soc. 151 (2004) A1077–A1083.
[59] B. Zhang, F. Xie, S.J. Hao, M. Sun, F.Y. Diao, R.S. Cai, Y.Q. Wang, Effect of annealing atmosphere on the phase composition and electrochemical properties of iron-based electrospun nanofibers, J. Energy Storage 124 (2025) 116851.
[60] J.L. Li, L. Shen, Z.N. Cheng, J.D. Zhang, L.X. Li, Y.T. Zhang, Y.B. Gao, C. Guo, X. Chen, C.Z. Zhao, R. Zhang, Q. Zhang, Unveiling solid-solid contact states in all-solid-state lithium batteries: an electrochemical impedance spectroscopy viewpoint, J. Energy Chem. 101 (2025) 16–22.